

1 Simulated Long-term Evolution of the Thermosphere during the 2 Holocene: 2. Circulation and Solar Tides

3 Xu Zhou^{1,3}, Xinan Yue^{1,2,3}, Yihui Cai^{1,2,3}, Zhipeng Ren^{1,2,3}, Yong Wei^{1,2,3}, Yongxin Pan^{1,2,3}

4 ¹Key Laboratory of Earth and Planetary Physics, Institute of Geology and Geophysics, Chinese Academy of Sciences, Beijing,
5 100029, China

6 ²College of Earth and Planetary Sciences, University of Chinese Academy of Sciences, Beijing, 100029, China

7 ³Beijing National Observatory of Space Environment, Institute of Geology and Geophysics, Chinese Academy of Sciences,
8 Beijing, 100029, China

9 *Correspondence to:* Xinan Yue (yuexinan@mail.iggcas.ac.cn)

10 **Abstract.** On timescales longer than the solar cycle, long-term changes in CO₂ concentration and geomagnetic field have the
11 potential to affect thermospheric dynamics. In this paper, we investigate the thermospheric dynamical response to these two
12 factors during the Holocene, using two sets of ~12,000-yr control runs by the coupled thermosphere-ionosphere model,
13 GCITEM-IGGCAS. The main results indicate that increased/decreased CO₂ will enhance/weaken the thermospheric
14 circulation throughout the Holocene, but this effect is nonlinear. The cooling effect of CO₂ in the thermosphere further
15 provides plausible conditions for atmospheric tidal propagation and increases the thermospheric tidal amplitude. Geomagnetic
16 variations induce hemispheric asymmetrical responses in the thermospheric circulation. Large changes in the circulation occur
17 at high latitudes in the hemisphere with distant magnetic poles drift, inferring a crucial role of geomagnetic non-dipole
18 variations in circulation changes. A positive correlation between the diurnal migrating tide (DW1) and geomagnetic dipole
19 moment is revealed for the first time. The amplitude of DW1 in temperature will increase by ~1–3 K for each 1×10^{22} Am²
20 increase in dipole moment.

21 1 Introduction

22 The main external energy input to the terrestrial thermosphere is solar radiation, particularly in the extreme ultraviolet (EUV)
23 band. The solar-driven circulation manifests as the flow across the isobars, in contrast to the geostrophic flow that dominates
24 in the middle and lower atmosphere (Forbes, 2007). This is because the Coriolis force is much smaller than the pressure
25 gradient term for the typical terrestrial thermosphere. Under absorption of solar daily-cyclic forcing, the atmosphere also
26 induces the solar tides, which refers to global-scale perturbations in atmospheric parameters with periods and zonal wave
27 numbers that are harmonics of a day and a zonal cycle. In addition to the local absorption of EUV radiation as the major source,
28 the solar tides in the thermosphere also come from upward propagating waves excited in the middle and lower atmosphere,
29 including the infrared absorption by tropospheric H₂O and ultraviolet absorption by stratospheric O₃ (Forbes and Zhang,
30 2022). Thus, the level of solar activity is expected to have a key impact on the dynamical variability in the thermosphere

31 (Oberheide et al., 2009; Sun et al., 2022). However, when inspecting on time scales longer than the solar cycle, the influence
32 from other secular variables, such as long-term changes in CO₂ concentration and main geomagnetic fields, should not be
33 ignored. It is then natural to ask how and to what extent these factors act on the thermospheric dynamics on long-term time
34 scales, e.g., since the beginning of the Holocene.

35
36 CO₂ plays a significant role in cooling the thermosphere, in contrast to the warming effect in the troposphere (Laštovička et
37 al., 2006; Solomon et al., 2018). Since the first prediction by Roble & Dickinson (1989), many observational evidences and
38 simulation experiments have been subsequently proposed to support the CO₂ cooling effect using modern techniques and
39 advanced models (Akmaev & Fomichev, 2000; Akmaev et al., 2006; Marsh et al., 2013; Ogawa et al., 2014; Qian et al., 2011;
40 2006; Solomon et al., 2015; Zhang et al. 2016). A well-established consensus is that every 10 ppm increase in CO₂
41 concentration will result in a ~1–3K decrease in global-mean temperature in the thermosphere (e.g. Solomon et al., 2018). As
42 the issue of increasing CO₂ becomes urgent (IPCC, 2014), researchers have also worked to elucidate the concomitant effects
43 on the upper atmosphere (Zhou et al., 2022), and one of which is the thermospheric dynamics. Using the GAIA (Ground-to-
44 topside Atmosphere Ionosphere model for Aeronomy) simulation, Liu et al. (2020) suggested that the doubling of CO₂
45 concentration should strengthen thermospheric meridional circulation, enhance diurnal migrating tide, and weaken semidiurnal
46 migrating tide. Kogure et al. (2022) further analyzed the underlying mechanism of the thermospheric zonal mean wind
47 response, suggesting that the ion drag, molecular viscosity, and meridional pressure gradient forces as the three main factors
48 are in the combined modulation. However, the impact of CO₂ on the long-term evolution of the thermospheric dynamics
49 during the Holocene is still poorly understood.

50
51 The secular variation of the geomagnetic field would produce considerable changes in the thermosphere temperature other
52 than the CO₂ effect. Although the geomagnetic variation does not act directly on the neutral atmosphere, it affects ion motion
53 and thus ionospheric behavior (Cai et al., 2019; Elias et al., 2022; Yue et al., 2018; Zossi et al., 2018), which are coupled to
54 the neutral atmosphere via ion-neutral collisions. The strength of the geomagnetic field determines the gyrofrequency and the
55 ionospheric conductivity, thus influencing the Joule heating power and $\mathbf{E} \times \mathbf{B}$ drift velocities (Cnossen et al., 2012; Zhou et al.,
56 2021). The geomagnetic tilted angle controlling the geographic distribution of the Joule heating should produce further changes
57 in temperature and neutral winds (Cnossen & Richmond, 2012). The secular changes of geomagnetic field produce regionally
58 both positive and negative changes, therefore in the global average their effect is negligible (Qian et al., 2021). Cnossen (2014)
59 reported that the geomagnetic variation over the last century could cause a ~±10K change in the thermosphere temperature
60 regionally, comparable to the –8K decrease in global temperature due to increased CO₂ over the same period. Analyses of
61 recent decades (Cnossen et al., 2020) and projections in the coming decades (Cnossen et al., 2022) about the thermospheric

62 climate change confirm the importance of the geomagnetic variation, although accelerating CO₂ growth still plays a dominant
63 role. Since the geomagnetic field has undergone a more complex evolution during the Holocene than in the present century
64 (Korte et al., 2011), the impact on the evolution of thermospheric dynamics is expected to be more dramatic and therefore
65 worth investigating.

66

67 The aim of the present study is to discuss the scenario of thermospheric dynamic changes due to the long-term changes in CO₂
68 concentration and geomagnetic field during the Holocene. This paper is organized as follows: Section 2 will briefly introduce
69 the numerical simulation settings. Section 3 will show the main results of the simulations, then Section 4 discuss the scientific
70 key points. In the end, a short summary is given in Section 5.

71 **2 Model Description and Settings**

72 Attempting to understand the long-term evolution of thermospheric dynamics affected by these two factors in the Holocene,
73 we designed long-term time-slice simulations based on the Global Coupled Ionosphere-Thermosphere-Electrodynamics Model
74 developed at the Institute of Geology and Geophysics, Chinese Academy of Sciences (GCITEM-IGGCAS, Ren et al., 2009,
75 2010, 2011, 2020). Detailed model description and settings are referred to Yue et al. (2022) and Cai et al. (2023), which have
76 carefully investigated the global thermal structure and density profile of the thermosphere and ionosphere, respectively. Here,
77 we give a briefly introduction to restate and to add key information. This 3-dimensional coupled thermosphere-ionosphere
78 model self-consistently solves the global thermospheric and ionospheric behavior in the altitudinal coordinate, covering
79 altitudes from 90 km to 600 km. The ionospheric electro-dynamics is solved on the provided geomagnetic field configuration
80 using magnetic apex coordinates (Richmond, 1995) based on a set of spherical harmonic coefficients. The calculation scheme
81 requires the geomagnetic field to be dipole-dominated, so the situation of geomagnetic reversal is difficult to portray. The
82 high-latitude electric potential and electric fields are specified by the empirical model of Weimer-96 (Weimer, 1996), which
83 is driven by the hemispheric power (HP), solar wind speed (SWS), interplanetary magnetic field (IMF), and cross-polar cap
84 potential (CPCP). At the lower boundary at 90 km, migrating tide in neutral temperature and density are given by the Global
85 Scale Wave Model (GSWM), while neutral winds are self-consistently calculated. Non-migrating tides are not included in this
86 study. The solar EUV radiation is described by the empirical model EUVAC (Richards et al., 1994), which is driven by the
87 proxy of solar flux at 10.7 cm (F10.7). The CO₂ cooling is calculated under the assumption of the nonlocal thermodynamic
88 equilibrium (NLTE) with a cooling-to-space approximation assumed. In this model, the CO₂ level is specified by a given value
89 for a fixed time under the assumption of diffusive equilibrium. This calculation formula follows Roble et al. (1988), and is
90 also adopted by other thermosphere-ionosphere coupled models, such as NCAR-TIEGCM (Qian et al., 2017).

91

92 To diagnose the long-term effects of CO₂ and geomagnetic field variations on the thermospheric dynamics, two control runs
93 (CR1 and CR2) were performed under perpetual solar minimum and geomagnetic quiet condition, which correspond to the
94 CR2 and CR1 in the Yue et al. (2022) and Cai et al. (2023). The driving parameters in Weimer-96 model are set as HP =
95 10GW, SWS = 300 m/s, IMF B_y = 0 nT, IMF B_z = -0.5 nT, and CPCP = 20 kV for both cases, representing the extreme
96 geomagnetically quiet condition of K_p = ~0.3. To eliminate the impact of solar variation, each case was performed under solar
97 minimum, correspondingly the F10.7 setting to be constant of 87sfu (solar flux unit, 1 sfu = 10⁻²² W m⁻² Hz⁻¹). In CR1, realistic
98 CO₂ from a combined dataset drives the GCITEM-IGGCAS model with a fixed configuration of geomagnetic fields. Hence,
99 the simulated variability of the thermosphere is derived exclusively from the CO₂ changes. The CO₂ dataset consists of three
100 components: (1) Estimation from the ice cores recorded air composition ~~in the interval of since~~ ~80,000 yrs before the present
101 ~~~1650~~ with a rough resolution of ~100 yrs during the Holocene (Lüthi et al., 2008). (2) Measurement in ice with high precision
102 back to 2000 yrs before the present (MacFarling Meure et al., 2006). (3) Modern atmospheric measurement at Mauna Loa
103 Observatory, Hawaii, since 1958 (Keeling et al., 1995). In CR2, the CO₂ level is fixed to be 270 ppm, corresponding to the
104 averaged value during the Holocene, while the geomagnetic fields are set to be varied with time. The specified geomagnetic
105 field before 1900 is provided by the CALS10k.2 model developed by Constable et al. (2016), which is based on the archeo-
106 magnetic and lake sediment data. Generally, this model roughly has spherical harmonics to degree and order of 10, and cubic
107 B-splines parameterization is implemented with knots positioned every 40 yrs. After 1900, the geomagnetic fields are described
108 by the International Geomagnetic Reference Field (IGRF) model (Alken et al., 2021). This model is based on the modern
109 magnetic observations to describe the spatial distribution of geomagnetic fields by the spherical harmonic degree and order of
110 13 with the time resolution of 5 yrs. The secular variation of geomagnetic field implemented in the CR2, including the dipole
111 moment and the position of magnetic and geomagnetic pole, was illustrated in Figure 1 of Yue et al. (2022), and the readers
112 could refer to Constable et al. (2016) for more detailed information. A general scenario includes: a) the dipole moment
113 fluctuated within 6.1–10.1 (10²²AM²), and has continuously decreased since 1700 by ~13%. b) The geomagnetic/magnetic
114 pole located at latitudes larger than 78°/70°, and drifted from the western hemisphere to the eastern hemisphere over the past
115 century. Both cases were run every 100 yrs in the period of 9455 BC to 1945 AD, and an additional run of 2015 AD was for
116 the contemporary condition. Particularly, pre-runs of 15 days were performed as spin-up preparation to eliminate the influence
117 from the initial conditions, and the outputs in the last day were used for analysis. Each case was running in two seasons, March
118 and June, with the aim of discussing the seasonal dependence of the thermospheric dynamical response.

119 3 Results

120 3.1 CO₂ effect

121 According to the CR1 results, Figure 1 illustrates the changes in zonal-mean winds due to increased CO₂ from 1945 to 2015
122 (310 to 400 ppm), exemplifying how the changes in CO₂ act on the thermospheric circulation. Figures 1b–1d show the
123 strengthening of the thermospheric circulation in March, mainly including enhanced equatorward flow from the north and
124 south poles, accelerated eastward flow at mid- and low-latitudes latitudes, and increased downward/upward movement in the
125 upper/lower thermosphere. The acceleration of the eastward zonal and equatorial meridional winds ~~winds~~ is about ~1–2 m/s
126 when CO₂ is increased by ~90 ppm. The CO₂ acceleration effect of the thermospheric ~~er~~reic circulation is also evident in June.
127 Figures 1f–1h show the enhanced summer-to-winter prevailing wind and corresponding increased westward/eastward zonal
128 wind in the summer/winter hemisphere due to the Coriolis force. The vertical winds also show a downward increase in the
129 upper thermosphere, while the slight increase in the lower thermosphere disappears around the winter pole. Compared to the
130 wind change in March, the accelerated thermospheric winds in June achieve ~2–3 m/s in zonal and meridional, and a few cm/s
131 in vertical. Our simulation gives a reasonable and convincing result compared to the GAIA simulation of Liu et al. (2020),
132 which shows an increase in the meridional winds of 5–15 m/s when CO₂ increases by 345 ppm.

133

134 Examining the CO₂ effect on the thermospheric circulation throughout the Holocene, Figure 2 illustrates the time evolution of
135 changes in meridional wind versus latitudes in the CR2 simulation. The chosen height of ~197 km is where the changes in the
136 meridional wind are significant as shown in Figure 1. The result for the beginning year (–9455) have been subtracted in order
137 to show the CO₂ effect more intuitively. The corresponding CO₂ variation is plotted in red-solid line, which is also subtracted
138 the CO₂ level in the beginning year (264 ppm). Changes in the meridional circulation are obviously highly correlated with
139 CO₂ variation, and become much more significant since ~1800 when the increase in CO₂ was much larger due to the industrial
140 revolution. The correlation coefficient is generally over ±0.99 at most latitudes. During the equinox season, the meridional
141 circulation ~~varied to be much equatorward/poleward~~ tends to be more/less equatorward due to the increase/decrease of CO₂.
142 As for the solstice season, the CO₂ effect manifests to be acceleration/deceleration of the summer-to-pole circulation. For the
143 past over 10,000 years before ~1800, the change in meridional circulation velocity in March and June only fluctuated by ±
144 0.4±0.1 m/s and –0.6–0.2 m/s, respectively. However, in the last 200 years, the CO₂-induced changes in meridional wind
145 could reach more than 1 m/s. Figure 3 further analyses the CO₂ effect on the thermospheric dynamics, choosing the averaged
146 zonal circulation as a proxy. The results show that CO₂ enhances the eastward flow at the equator during March, rather than
147 being strictly linear. The growth of the accelerated eastward flow becomes small as CO₂ increases. Linear regressions show a
148 change of 0.012 m/s in the thermospheric equatorial zonal flow per ppm CO₂ increase, and the parabolic fit should be in good
149 agreement with the simulated data. The parabolic fitting obviously indicates that the rate of change of the thermospheric

150 circulation slows down at the present CO₂ level. A similar nonlinear effect is also manifested in the June zonal circulation
151 (Figure 3c).

152

153 As for the solar tidal response to the CO₂ variation during the Holocene, Figure 4 illustrates the time evolution of diurnal
154 migrating tide in temperature (DW1-T) at ~240 km, which is the major tidal component in the thermosphere. The DW1-T tidal
155 amplitude is positively correlated with CO₂ changes, manifesting as increasing by ~10 K compared with the beginning year
156 (-9455) during March when the CO₂ level achieve 400 ppm in the modern era, particularly maximizing at the equatorial and
157 low-latitude region. From 8000 BC to 4000 BC, when the CO₂ level was low throughout the Holocene, the DW1-T amplitude
158 also decreased slightly. The specified DW1-T amplitude at the lower boundary in March is a maximum of ~16 K at the equator
159 and two secondary peaks of ~7 K at $\pm 35^\circ$. As for the DW1-T at the lower boundary in June, the strength is about ~1/2 of that
160 during March. Correspondingly, the changes in the thermospheric DW1-T amplitude in the modern era are slightly over 2 K,
161 only ~1/4 ~~of that~~ that in March. The maximum change is found at mid-latitudes in the winter hemisphere, rather than the
162 equator. The latitudinal difference in the DW1-T changes is contrary with the DW1-T time tendency, which generally
163 maximizes in the summer hemisphere (Gu & Du, 2018).

164 3.2 Geomagnetic field effect

165 The geomagnetic field effect on the thermospheric circulation is regional and complicated, unlike the global effect of CO₂.
166 Figure 5 exemplified the thermospheric circulation in the present era in the CR2 simulation, and manifested how the circulation
167 changed over the past 70 years due to the geomagnetic variation. The thermospheric winds generally flow across the isotherm
168 due to the pressure gradient force and can maximize over 100 m/s around the terminator. The auroral heating modulates the
169 solar-driven winds and decreases the poleward flow at high- and mid-latitudes. Figure 5b shows that the geomagnetic variation
170 from 1945 to 2015 alters the geographic distribution of temperature in March, notably at high latitudes ($\sim \pm 15$ K) and not
171 negligibly at mid- and low-latitudes (± 5 K). Correspondingly, the change in horizontal neutral winds could exceed 30 m/s at
172 high latitudes and around the dusk sector. The changes in temperature and wind induced by the geomagnetic field are smaller
173 in June than that in March, which is about ± 10 K/ ± 3 K at high/mid-low latitudes for temperature and maximizes ~20 m/s for
174 horizontal winds. The circulation change shows a larger change in the northern hemisphere ~~is much larger than~~ in the southern
175 hemisphere, ~~regardless during in both simulations for~~ March ~~and~~ June. The horizontal wind changes in the southern
176 hemisphere are generally smaller by 10–20 m/s than that in the northern hemisphere, and the temperature change is smaller by
177 5–10 K. The hemisphere difference is coincident with the asymmetrical change in the geomagnetic poles. The northern
178 magnetic pole shifted 12° and 76° in latitude and longitude, respectively. However, the southern magnetic pole drifted by
179 merely 4° and 7° in latitude and longitude, respectively.

180

181 In addition, Figures 5b and 5d show that the geomagnetic variation during the period 1945–2015 induced different temperature
182 responses during the daytime/nighttime at mid- and low-latitudes. This local-time-dependent effect is further examined in
183 Figure 6 and Figure 7 for the month of March and June, respectively. Figure 6a illustrates the local-time dependence of
184 temperature changes due to the geomagnetic variation with respect to the beginning year of 9455 BC, when the dipole moment
185 of the geomagnetic field underwent a minimum period. During the daytime, the average temperature at low-latitude was
186 generally higher than in 9455 BC for most of the time, except for 4900 BC and 4700 BC. The changed magnitude varied from
187 -2 K to 9 K. In contrast, the nighttime temperature change is negative compared to 9455 BC since 3100 BC, and ranges from
188 -7 K to $+6$ K before 3100 BC. We then deduced the day-night differences in the temperature response at mid- and low-latitudes
189 and illustrated them in comparison with the strength of the geomagnetic dipole moment in Figure 6b. The results show an
190 obviously positive correlation between the day-night differences and the geomagnetic dipole moment, indicating that a stronger
191 geomagnetic dipole moment would induce larger day-night temperature differences in the thermosphere at mid-to-low latitudes
192 in March, thereby exacerbating the prevailing day-to-night flow. During the whole simulation period in the Holocene, the day-
193 night difference in temperature caused by the geomagnetic variation can vary up to ~ 15 – 20 K. The fluctuation magnitude is
194 about 5% ~~relative to concerning~~ the typical day-night temperature difference in the thermosphere ~~is generally of~~ 300–400 K.
195 Meanwhile, the geomagnetic dipole moment varies more than 40%. As for the case of June, the positive correlation is not valid
196 for all latitudes and becomes more complicated. As the dipole moment increases, the average temperature at low-latitudes
197 decreases for both daytime and nighttime. The change in the day-night temperature difference is weaker than that in March.
198 Around the equator and in the southern mid-latitudes, the day-night difference in temperature decreases while the geomagnetic
199 dipole moment increases, such as during 8000–6600 BC and 2600 BC–1600 AD.

200

201 As mentioned above, the daytime temperature responses in the thermosphere differed from that of the nighttime due to the
202 geomagnetic variation, suggesting that the tidal response should also be affected, especially during March. Figure 8 then
203 examines the thermospheric tidal response to the geomagnetic variation during the Holocene in the CR2 simulation, including
204 the diurnal and semidiurnal migrating tides in temperature (DW1-T and SW2-T). These two major tidal components respond
205 differently to the geomagnetic variation. The strength of DW1-T is positively correlated with the geomagnetic dipole moment.
206 When the dipole moment intensity becomes $\sim 40\%$ larger than at the beginning of the simulation, the amplitude of DW1-T
207 increases correspondingly by ~ 10 K. However, the SW2-T around the equator is negatively correlated to the geomagnetic
208 dipole moment, while at mid-latitudes it is positively correlated. The strength of SW2-T response to the geomagnetic variation
209 is much smaller than that of DW1-T, and ranges within $\sim \pm 2$ K throughout the simulation period in the Holocene. Figure 9
210 further diagnoses the relationship between the thermospheric migrating tides and the geomagnetic dipole moment for different

211 thermospheric altitudes versus latitudes. A linear regression between the tidal amplitude and geomagnetic dipole moment is
212 calculated. Figures 9a and 9b illustrate the estimated coefficient for the linear regression in the altitude-latitude plane, with
213 regions where the absolute value of the correlation coefficient is less than 0.6 being masked. The results show that as the
214 geomagnetic dipole moment increases per 10^{22}AM^2 the thermospheric DW1-T in March would enhance by 1–3 K, with two
215 maximums around $\pm 30^\circ$ – 40° . The response of SW2-T is much smaller and insignificant. At the equator, the increase in
216 geomagnetic dipole moment by 10^{22}AM^2 would lessen the SW2-T amplitude merely by ~ 0.3 K. A slight enhancement of SW2-
217 T due to the increase in geomagnetic dipole moment could be found in the upper thermosphere at mid-latitudes, while the
218 growth rate is only ~ 0.4 K/ 10^{22}AM^2 .

219 4 Discussion

220 In this paper, two control runs, CR1 and CR2, were conducted to examine the response of thermospheric dynamics to long-
221 term changes in CO₂ and geomagnetic field during the last 12,000 years of the Holocene. The CO₂ effect was revealed as an
222 enhancement of the general circulation with increasing CO₂ levels (Figure 1–2), which agreed with the result of Liu et al.
223 (2020). Rind et al. (1990) also found that an increase in CO₂ similarly enhanced the mesospheric circulation. Both of them
224 suggested that the increased eddy forcing and gravity waves (GWs) should play an important role. However, the GCITEM-
225 IGGCAS model does not involve a parameterization scheme for GWs because the GWs mainly affect the mean flow in the
226 mesosphere rather than in the thermosphere. Therefore, the changes in the circulation caused by CO₂ variations in our results
227 cannot be attributed to GWs. The interpretation by Kogure et al. (2022) should be responsible for the fact that the changes in
228 ion drag, molecular viscosity, and meridional pressure gradient forces are in the combined modulation. An interesting finding
229 is that the CO₂ increase does not linearly accelerate the circulation and tends to be “saturated” as shown in Figure 3. The
230 plausible explanation is that the molecular viscosity is non-linearly related to the temperature. As for the tidal response to the
231 CO₂ effect, the DW1 amplitude is positively correlated with CO₂ variation (Figure 4). A reasonable deduction is that the
232 decreased viscosity due to the enhanced CO₂ cooling should be less likely to dissipate tidal propagation from below. The
233 latitudinal structure of the DW1 response to CO₂ differs from that of Liu et al. (2020), partly because their results mixed the
234 influences of changes in tidal sources from below, whereas our results reflected the internal thermospheric responses. In
235 addition, this paper only considered the geomagnetically quiet condition, while the efficiency of CO₂ forcing somewhat differs
236 under low and high geomagnetic activity conditions according to GAIA simulations by Liu et al. (2021).

237
238 Figure 5 illustrated an asymmetric response in circulation to the geomagnetic variation. The change in neutral winds was larger
239 in the hemisphere with a more distant geomagnetic pole shift. Given the variation in the dipole component of the geomagnetic
240 field is hemispherical symmetric, it could logically infer that the hemisphere difference in circulation is contributed by the

241 variation of the non-dipole component. The neutral temperature change due to geomagnetic variation has a similar pattern to
242 the ion temperature in Cnossen et al. (2014), which is also manifested to decrease around the daytime equatorial ionization
243 anomaly (EIA) peaks. A possible causal linkage could be proposed that the geomagnetic variation affected the equatorial
244 plasma drift velocity, and then redistributed the electron density around the EIA region. As the electron density becomes
245 large/small the electron temperature changed conversely. The ion temperature change then should be more or less related to
246 the electron temperature change. Generally, the smaller strength of the geomagnetic fields would induce stronger equatorial
247 ~~$\mathbf{E} \times \mathbf{B}$ -vertical drift ($\mathbf{E} \times \mathbf{B}/B^2$)~~ and thus increase the electron density at the EIA peaks, and Yue et al. (2022) confirmed such a
248 relationship. During the nighttime, the equatorial drift tended to be downward and the EIA structure disappeared in general.
249 So, the above-discussed causality is not valid and the nighttime neutral temperature response should be different. The increased
250 Joule heating related to the weakening of the geomagnetic field might be responsible. Hence, the geomagnetic variation would
251 redistribute the temperature in the daytime and nighttime differently (Figure 6), then caused the day-night difference in Figures
252 6 and 7. The seasonal dependence of the day-night difference in temperature response to the geomagnetic variation is still
253 puzzled and needs further explanation in the future. The temperature redistribution due to geomagnetic variation then causes
254 the tidal responses in Figures 8 and 9. At mid-latitudes, both DW1 and SW2 manifest to be positively correlated to the ~~dipole~~
255 ~~dipole~~ moment, partly because the ~~strengthen geomagnetic field leading to the lower cooler~~ thermosphere caused by
256 strengthening geomagnetic field (Cai et al., 2023) modulated the tidal propagation from below. At the low-latitudes, the effect
257 from $\mathbf{E} \times \mathbf{B}$ drift at daytime becomes important as aforementioned, therefore different from that in mid-latitudes.

258
259 As a tentative investigation of the long-term change of thermospheric dynamics during ~12,000 yrs, this paper still has some
260 limitations and flaws, and one of them is the fixed lower boundary. In the present work, the migrating tides at the lower
261 boundary (90 km) are set to be unvaried regardless of simulating different periods in the Holocene. To our knowledge, the
262 long-term trend around mesopause is still debated, and the understanding changed from no trend to a mild negative trend in
263 general (Beig, 2003; Huang et al., 2014; Laštovička, 2017). This is partly because the temperature trends at these heights are
264 sensitive to the changes in stratospheric ozone concentration (Lübken et al., 2013). A whole atmosphere simulation performed
265 by Solomon et al (2018) also indicated there are very weak trends in the mesopause region. Hence, the perpetual lower
266 boundary should be a conservative and compromised treatment, additionally considering little evidences have been provided
267 on how the atmospheric tides change during such a long-term historical time. Besides, the fixed lower boundary inferred that
268 the tidal source from the lower atmosphere is constrained to be unvaried, so our results mainly describe the effect of
269 propagation conditions and local excitation on the long-term dynamics change in the thermosphere. In the next step, simulation
270 based on a whole atmosphere climate model, like the WACCM-X (Liu et al., 2018) and GAIA (Jin et al., 2011), should give

271 a much more realistic scenario of the long-term change in the thermospheric dynamics, nevertheless, the computation cost will
272 increase substantially.

273

274 In addition, the empirical model describing the high-latitude input, Weimer-96, is based on modern satellite measurements.
275 Although the geomagnetic intensity variation did not take into consideration, the effect of the geomagnetic tilted angle is
276 included in the model. The drift of magnetic poles and aurora region is thus considered given the Weimer-96 is based on a
277 magnetic coordinate. The intensity of the geomagnetic field is examined to influence the magnetosphere configuration and
278 thus expected to affect the energy input to the high-latitude thermosphere (Zhong et al., 2014; Cnossen et al., 2012). Vogt et
279 al. (2009) summarized the potential impact of the geomagnetic field variation on the geospace by modulating the shielding of
280 the energetic charged particles. During the simulated period, the dipole moment (M) is in the $6 \times 10^{22} - 1 \times 10^{23}$ Am² range. As
281 the sine of polar cap size (θ) is generally proportional to $M^{-1/6}$, a rough estimation deduces that θ would change by $\sim 3^\circ$, within
282 latitudinal resolution (5°) in the model. Theoretical scaling about cross-polar cap potential (Φ), $\Phi \propto M^{1/3}$, inferring that the Φ
283 should varied from 18 to 21 kV during the Holocene if we set the Φ as 20 kV at the present era. Comparing a typical
284 geomagnetically disturbed condition that Φ is ~ 80 kV for Kp = 4, the relative change in Φ above is quite small. Cnossen et al.
285 (2014) also declared that the magnetosphere-ionosphere coupling only significantly during the disturbed conditions. Given our
286 simulation is perpetually geomagnetically quiescent, the impact of geomagnetic variation on the high-latitude energy input
287 should be limited.

288

289 In this work, the CO₂ and geomagnetic fields were regarded as two independent external driving to the simulation regardless
290 of their interaction, although whether the interaction exists is still controversial. Zhou et al. (2021) proposed that the decrease
291 in geomagnetic intensity would redistribute the CO₂ in the upper atmosphere using the whole atmosphere simulation. Their
292 investigation suggested that the increased ionospheric conductivities due to the weakened geomagnetic intensity would induce
293 much more Joule heating to warm the high-latitude lower thermosphere, which then should enhance the upwelling flow and
294 bring rich CO₂ from below. This result is based on the physical fact that the CO₂ distribution becomes deviated from the well-
295 mixed equilibrium above the mesopause ($\sim 80-90$ km) and the time scale of eddy diffusion becomes much larger in the upper
296 atmosphere (Beagley et al., 2010; Rezac et al., 2015), so that the dynamical processes could modulate the CO₂ distribution.
297 However, up to date, little observational evidence has been proposed to support the possible link between CO₂ and
298 geomagnetic fields. A simulation project conducted by the whole atmosphere model in the next step could provide more
299 information.

300

301 Responses of the non-migrating tides to the variation of CO₂ and geomagnetic fields were not considered in this paper. The
302 eastward propagating diurnal tides with a zonal wave number of 3 (DE3) should be not much sensitive to the CO₂ change,
303 according to the discussion by Liu et al. (2020). This result was expected as the longitudinal variation of CO₂ concentration
304 is generally not obvious. On the other hand, geomagnetic fields crucially influence the non-migrating tidal propagation in the
305 upper atmosphere, through the electro-dynamo or parallel-line transport. For example, Jiang et al. (2018) revealed that DE3
306 tide can induce the longitudinal wavenumber-3 (WN3) structure rather than the should-be WN4 structure through the electro-
307 dynamical coupling with the geomagnetic field. Zhang et al. (2020) proposed that the significant role of parallel-line transport
308 alters the interhemispheric symmetry as the enhanced planetary waves upward propagated during the 2009 sudden stratosphere
309 warming (SSW) event. As the realistic geomagnetic field is much more complicated than the dipole or tilted dipole, a given
310 non-migrating tides propagating into the thermosphere would broaden the spectra of wavenumber. Yue et al. (2013) found that
311 there were complicated longitudinal structures rather than simply the WN3 as the quasi-2-day wave with westward zonal
312 wavenumber 3 propagating into the upper atmosphere. In this future work, the non-migrating tidal response to the long-term
313 variation will be worth studying.

314 5. Conclusions

315 This paper diagnosed the long-term changes in the thermospheric dynamics caused by the secular variation of CO₂ emissions
316 and geomagnetic field during the Holocene, using the global coupled thermosphere-ionosphere model, GCITEM-IGGCAS.
317 Two sets of long-term time-slice simulation covering ~12,000 yrs were performed by independently controlling the CO₂ level
318 and the configuration of geomagnetic fields, both under the perpetual condition of solar minimum and geomagnetic quiescence.
319 The corresponding changes in the circulation and major solar tides in the thermosphere were then analyzed, and the main
320 results were summarized as follows:

321 1. The CO₂ increase/decrease generally strengthened/weakened the general circulation in the thermosphere ~~simultaneously,~~
322 and notably the circulation has intensified dramatically with a dramatic strengthen in the circulation as the steep increase in
323 CO₂ ~~steeply increases~~ since the industrial revolution. The circulation increase due to the CO₂ variation was ~~examined~~ found
324 ~~to be grow~~ non-linearly ~~growth~~, which is expected to be caused by the nonlinear relationship between temperature and
325 molecular viscosity.

326 2. The amplitude of the diurnal migrating tide in the thermosphere will strengthen as the CO₂ increases throughout the
327 Holocene because the increased CO₂ cooling provides a plausible condition for tidal propagation.

328 3. Secular variation of geomagnetic field have a regional impact on the thermospheric circulation, particularly pronounced at
329 high latitudes and around the dusk sector. The prominent hemispheric differences in the thermospheric circulation response
330 infer a crucial role of the geomagnetic non-dipole component.

331 4. Geomagnetic variations also redistribute neutral temperature at mid- and low-latitudes and lead to different responses in the
332 daytime and nighttime, which then influence the thermospheric dynamics.

333 5. The geomagnetic dipole moment is highly correlated with DW1 tidal amplitude at mid- and low-latitudes during March,
334 and an enhancement of 1×10^{22} Am² will cause an increase in $\sim 1\text{--}3$ K of DW1-T in the thermosphere.

335 **Data availability**

336 The spherical harmonic coefficients of CALS10k.2 model was obtained from the website: <https://earthref.org/ERDA/2207>.

337 The IGRF model was downloaded from the website: <https://www.ngdc.noaa.gov/IAAGA/vmod/igrf.html>. The Antarctica

338 Vostok and EPICA Dome C ice cores CO₂ level was derived from the website: [https://data.noaa.gov/dataset/dataset/noaa-](https://data.noaa.gov/dataset/dataset/noaa-wds-paleoclimatology-aicc2012-800kyr-antarctic-ice-core-chronology)

339 [wds-paleoclimatology-aicc2012-800kyr-antarctic-ice-core-chronology](https://data.noaa.gov/dataset/dataset/noaa-wds-paleoclimatology-aicc2012-800kyr-antarctic-ice-core-chronology). The Antarctica Law Dome ice core CO₂ data was

340 downloaded from the website: <https://www.ncei.noaa.gov/access/metadata/landing-page/bin/iso?id=noaa-icecore-9959>. The

341 Mauna Loa observed CO₂ was from the website: <https://gml.noaa.gov/ccgg/trends/data.html>. The simulated data by GCITEM-

342 IGGCAS model under different control runs are available at: <http://doi.org/10.17605/OSF.IO/ZQ8HY>.

343 **Acknowledgments**

344 The authors acknowledge the support of the B-type Strategic Priority Program of the Chinese Academy of Sciences (Grant

345 XDB41000000), the Project of Stable Support for Youth Team in Basic Research Field, CAS (YSBR-018), the National

346 Natural Science Foundation of China (41621004, 42241106, 42204165), the CAS Youth Interdisciplinary Team (JCTD-2021-

347 05), and the Key Research Program of the Institute of Geology and Geophysics, CAS (Grant IGGCAS-201904).

348 **References**

349 Akmaev, R. A., and Fomichev, V. I.: A model estimate of cooling in the mesosphere and lower thermosphere due to the CO₂
350 Increase over the last 3–4 decades, *Geophys. Res. Lett.*, 27(14), 2113–2116,
351 <https://doi.org/https://doi.org/10.1029/1999GL011333>, 2000

352 Akmaev, R. A., Fomichev, V. I., and Zhu, X.: Impact of middle-atmospheric composition changes on greenhouse cooling in
353 the upper atmosphere, *J. Atmos. Sol.-Terr. Phys.*, 68(17), 1879–1889,
354 <https://doi.org/https://doi.org/10.1016/j.jastp.2006.03.008>, 2006

355 Alken, P., Thébault, E., Beggan, C. D., Amit, H., Aubert, J., Baerenzung, J., Bondar, T. N., Brown, W. J., Califf, S., Chambodut,
356 A., Chulliat, A., Cox, G. A., Finlay, C. C., Fournier, A., Gillet, N., Grayver, A., Hammer, M. D., Holschneider, M., Huder, L.,
357 Hulot, G., Jager, T., Kloss, C., Korte, M., Kuang, W., Kuvshinov, A., Langlais, B., Léger, J. M., Lesur, V., Livermore, P. W.,
358 Lowes, F. J., Macmillan, S., Magnes, W., Mandea, M., Marsal, S., Matzka, J., Metman, M. C., Minami, T., Morschhauser, A.,
359 Mound, J. E., Nair, M., Nakano, S., Olsen, N., Pavón-Carrasco, F. J., Petrov, V. G., Ropp, G., Rother, M., Sabaka, T. J.,
360 Sanchez, S., Saturnino, D., Schnepf, N. R., Shen, X., Stolle, C., Tangborn, A., Tøffner-Clausen, L., Toh, H., Torta, J. M.,
361 Varner, J., Vervelidou, F., Vigneron, P., Wardinski, I., Wicht, J., Woods, A., Yang, Y., Zeren, Z., and Zhou, B.: International

362 Geomagnetic Reference Field: the thirteenth generation, *Earth, Planets Space*, 73, 49, [https://doi.org/10.1186/s40623-020-](https://doi.org/10.1186/s40623-020-01288-x)
363 01288-x, 2021.

364 Beagley, S. R., Boone, C. D., Fomichev, V. I., Jin, J. J., Semeniuk, K., McConnell, J. C., and Bernath, P. F.: First multi-year
365 occultation observations of CO₂ in the MLT by ACE satellite: observations and analysis using the extended CMAM, *Atmos.*
366 *Chem. Phys.*, 10, 1133–1153, <https://doi.org/10.5194/acp-10-1133-2010>, 2010.

367 Beig, G., Keckhut, P., Lowe R. P., et al.: Review of mesospheric temperature trends, *Rev. Geophys.*, 41(4), 1015,
368 <https://doi.org/10.1029/2002RG000121>, 2003

369 Cai, Y., Yue, X., Wang, W., Zhang, S., Liu, L., Liu, H., & Wan, W.: Long-term trend of topside ionospheric electron density
370 derived from DMSP data during 1995–2017, *J. Geophys. Res.: Space*
371 *Phys.*, 124, 10708– 10727, <https://doi.org/10.1029/2019JA027522>, 2019

372 Cnossen, I.: The importance of geomagnetic field changes versus rising CO₂ levels for long-term change in the upper
373 atmosphere, *J. Space Weather Space Clim.*, 4, A18, <https://doi.org/10.1051/swsc/2014016>, 2014.

374 Cnossen, I.: A Realistic Projection of Climate Change in the Upper Atmosphere Into the 21st Century, *Geophys. Res. Lett.*,
375 49, e2022GL100693, <https://doi.org/10.1029/2022gl100693>, 2022.

376 Cnossen, I. and Maute, A.: Simulated Trends in Ionosphere-Thermosphere Climate Due to Predicted Main Magnetic Field
377 Changes From 2015 to 2065, *J. Geophys. Res.: Space Phys.*, 125, e2019JA027738, <https://doi.org/10.1029/2019ja027738>,
378 2020.

379 Cnossen, I., and Richmond, A. D.: How changes in the tilt angle of the geomagnetic dipole affect the coupled magnetosphere-
380 ionosphere-thermosphere system, *J. Geophys. Res. Atmospheres*, 117(A10), A10317, <https://doi.org/10.1029/2012JA018056>,
381 2012.

382 Cnossen, I., Richmond, A. D., and Wiltberger, M.: The dependence of the coupled magnetosphere-ionosphere-thermosphere
383 system on the Earth's magnetic dipole moment, *J. Geophys. Res.: Space Phys.*, 117, A05302,
384 <https://doi.org/10.1029/2012JA017555>, 2012.

385 Constable, C., Korte, M., and Panovska, S.: Persistent high paleosecular variation activity in southern hemisphere for at least
386 10 000 years, *Earth Planet. Sci. Lett.*, 453, 78-86, <https://doi.org/10.1016/j.epsl.2016.08.015>, 2016.

387 Elias, A. G., de Haro Barbas, B. F., Zossi, B. S., Medina, F. D., Fagre, M., and Venchiarutti, J. V.: Review of long-term trends
388 in the equatorial ionosphere due the geomagnetic field secular variations and its relevance to space weather, *Atmosphere*, 13,
389 40, <https://doi.org/10.3390/atmos13010040>, 2022.

390 Forbes, J. M.: Dynamics of the thermosphere, *Journal of the Meteorological Society of Japan*, 85, 193-213,
391 <https://doi.org/10.2151/jmsj.85B.193>, 2007.

392 Forbes, J. M., and Zhang, X.: Hough Mode Extensions (HMEs) and solar tide behavior in the dissipative thermosphere, *J.*
393 *Geophys. Res.: Space Phys.*, 127, e2022JA030962, <https://doi.org/10.1029/2022JA030962>, 2022.

394 Gu, H., and Du, J.: On the Roles of Advection and Solar Heating in Seasonal Variation of the Migrating Diurnal Tide in the
395 Stratosphere, Mesosphere, and Lower Thermosphere, *Atmosphere*, 9(11), 440, <http://dx.doi.org/10.3390/atmos9110440>, 2018.

396 Huang, F. T., Mayr, H. G., Russell, J. M., III, and Mlynczak, M. G.: Ozone and temperature decadal trends in the stratosphere,
397 mesosphere and lower thermosphere, based on measurements from SABER on TIMED, *Ann. Geophys.*, 32, 935–949,
398 <https://doi.org/10.5194/angeo-32-935-2014>, 2014.

399 IPCC: Climate Change 2014: Synthesis Report. Contribution of Working Groups I, II and III to the Fifth Assessment Report
400 of the Intergovernmental Panel on Climate Change [Core Writing Team, R.K. Pachauri and L.A. Meyer (eds.)]. IPCC, Geneva,
401 Switzerland, 151 pp., 2014.

402 Jiang, J., Wan, W., Ren, Z., and Yue, X.: Asymmetric de3 causes wn3 in the ionosphere, *J. Atmos. Sol.-Terr. Phys.*, 173, 14-
403 22, <http://dx.doi.org/10.1016/j.jastp.2018.04.006>, 2018.

404 Jin, H., Miyoshi, Y., Fujiwara, H., Shinagawa, H., Terada, K., and Terada, N., et al.: Vertical connection from the tropospheric
405 activities to the ionospheric longitudinal structure simulated by a new Earth’s whole atmosphere-ionosphere coupled model, *J.*
406 *Geophys. Res.*, 116(A1), A01316, <https://doi.org/10.1029/2010JA015925>, 2011.

407 Keeling, C. D., Whorf, T. P., Wahlen, M., & vander Plicht, J. : Interannual extremes in the rate of rise of atmospheric carbon
408 dioxide since 1980, *Nature*, 375(6533), 666–670, <https://doi.org/10.1038/375666a0>, 1995.

409 Kogure, M., Liu, H., and Tao, C.: Mechanisms for zonal mean wind responses in the thermosphere to doubled CO2
410 concentration, *J. Geophys. Res.: Space Phys.*, 127, e2022JA030643, <https://doi.org/10.1029/2022JA030643>, 2022

411 Korte, M., Constable, C., Donadini, F., and Holme, R.: Reconstructing the Holocene geomagnetic field, *Earth and Planetary*
412 *Science Letters*, 312(3–4), 497–505, <https://doi.org/10.1016/j.epsl.2011.10.031>, 2011

413 Laštovička, J., R. Akmaev, A., Beig, G., Bremer, J., and Emmert J. T.: Global change in the upper atmosphere, *Science*, 314,
414 1253-1254, <https://doi.org/10.1126/science.1135134>, 2006.

415 Laštovička, J.: A review of recent progress in trends in the upper atmosphere, *J. Atmos. Sol.-Terr. Phys.*, 163, 2-13,
416 <https://doi.org/10.1016/j.jastp.2017.03.009>, 2017.

417 [Liu, H., Tao, C., Jin, H., and Abe, T.: Geomagnetic activity effect on CO2-driven trend in the thermosphere and ionosphere:
418 Ideal model experiments with GAIA. *J. Geophys. Res.: Space Phys.*, 126\(1\), e2020JA028607,
419 <https://doi.org/10.1029/2020JA028607>, 2021.](https://doi.org/10.1029/2020JA028607)

420 Liu, H., Tao, C., Jin, H., and Nakamoto, Y.: Circulation and tides in a cooler upper atmosphere: Dynamical effects of CO2
421 doubling, *Geophys. Res. Lett.*, 47, e2020GL087413. <https://doi.org/10.1029/2020GL087413>, 2020

422 Liu, H.-L., Bardeen, C. G., Foster, B. T., Lauritzen, P., Liu, J., Lu, G., ... Wang, W.: Development and validation of the Whole
423 Atmosphere Community Climate Model with thermosphere and ionosphere extension (WACCM-X 2.0), *J. Adv. Model. Earth*
424 *Syst.*, 10, 381–402, <https://doi.org/10.1002/2017MS001232>, 2018

425 Lübken, F.-J., Berger, U., and Baumgartner, G.: Temperature trends in the midlatitude summer mesosphere. *J. Geophys. Res.:*
426 *Atmospheres*, 118, 13347–13360, <https://doi.org/10.1002/2013JD020576>, 2013.

427 Lüthi, D., Le Floch, M., Bereiter, B., Blunier, T., Barnola, J.-M., Siegenthaler, U., et al.: High-resolution carbon dioxide
428 concentration record 650,000–800,000 yr before present, *Nature*, 453, 379–382, <https://doi.org/10.1038/nature06949>, 2008.

429 MacFarling Meure, C., Etheridge, D., Trudinger, C., Steele, P., Langenfelds, R., van Ommen, T., et al.: Law Dome CO2, CH4,
430 and N2O ice core records extended to 2,000 yr BP, *Geophys. Res. Lett.*, 33, L14810, <https://doi.org/10.1029/2006GL026152>,
431 2006.

432 Marsh, D. R., Mills, M. J., Kinnison, D. E., Lamarque, J. F., Calvo, N., and Polvani, L. M.: Climate change from 1850 to 2005
433 simulated in CESM1(WACCM), *J. Climate*, 26(19), 7372–7391, <https://doi.org/10.1175/JCLI-D-12-00558.1>, 2013.

434 Neale, R. B., Richter, J., Park, S., Lauritzen, P. H., Vavrus, S. J., Rasch, P. J., and Zhang, M. H.: The mean climate of the
435 Community Atmosphere Model (CAM4) in forced SST and fully coupled experiments, *J. Climate*, 26(14), 5150–5168.
436 <https://doi.org/10.1175/JCLI-D-12-00236.1>, 2013.

437 Oberheide, J., Forbes, J. M., Häusler, K., Wu, Q., and Bruinsma, S. L.: Tropospheric tides from 80 to 400 km: Propagation,
438 interannual variability, and solar cycle effects, *J. Geophys. Res.: Atmosphere*, 114, D00I05,
439 <https://doi.org/10.1029/2009JD012388>, 2009.

440 Ogawa, Y., Motoba, T., Buchert, S. C., Häggström, I., and Nozawa, S.: Upper atmosphere cooling over the past 33 yr, *Geophys.*
441 *Res. Lett.*, 41, 5629–5635, <https://doi.org/10.1002/2014GL060591>, 2014

442 ~~[Qian, L. Y., Burns, A. G., Solomon, S. C., and Wang, W. B.: Carbon dioxide trends in the mesosphere and lower thermosphere,](#)~~
443 ~~[J. Geophys. Res.](#), 122(4), 4474–4488, <https://doi.org/10.1002/2016JA023825>, 2017.~~

444 Qian, L., Laštovička, J., Roble, R. G., and Solomon, S. C.: Progress in observations and simulations of global change in the
445 upper atmosphere, *J. Geophys. Res.: Space Phys.*, 116, A00H03, <https://doi.org/10.1029/2010JA016317>, 2011.

446 ~~[Qian, L., McInerney, J. M., Solomon, S. S., Liu, H., and Burns, A. G.: Climate changes in the upper atmosphere: Contributions](#)~~
447 ~~[by the changing greenhouse gas concentrations and Earth's magnetic field from the 1960s to 2010s,](#)~~ *J. Geophys. Res.: Space*
448 ~~[Phys.](#), 126(3), e2020JA029067, <https://doi.org/10.1029/2020JA029067>, 2021.~~

449 Qian, L., Roble, R. G., Solomon, S. C., and Kane, T. J.: Calculated and observed climate change in the thermosphere, and a
450 prediction for solar cycle 24, *Geophys. Res. Lett.*, 33, L23705, <https://doi.org/10.1029/2006gl027185>, 2006.

451 ~~[Qian, L. Y., Burns, A. G., Solomon, S. C., and Wang, W. B.: Carbon dioxide trends in the mesosphere and lower thermosphere,](#)~~
452 ~~[J. Geophys. Res.](#), 122(4), 4474–4488, <https://doi.org/10.1002/2016JA023825>, 2017.~~

453 Rezac, L., Jian, Y., Yue, J., Russell III, J. M., Kutepov, A., Garcia, R., Walker, K., and Bernath, P.: Validation of the global
454 distribution of CO₂ volume mixing ratio in the mesosphere and lower thermosphere from SABER, *J. Geophys. Res.*, 120(23),
455 12067–12081, <https://doi.org/10.1002/2015JD023955>, 2015

456 Ren, Z., Wan, W., and Liu, L.: GCITEM-IGGCAS: A new global coupled ionosphere–thermosphere–electrodynamics model,
457 *J. Atmos. Sol.-Terr. Phys.*, 71, 2064–2076, <https://doi.org/10.1016/j.jastp.2009.09.015>, 2009.

458 Ren, Z., Wan, W., Liu, L., and Xiong, J.: Simulated longitudinal variations in the lower thermospheric nitric oxide induced by
459 nonmigrating tides, *J. Geophys. Res.: Space Phys.*, 116, A04301, <https://doi.org/10.1029/2010ja016131>, 2011.

460 Ren, Z., Wan, W., Xiong, J., and Li, X.: A Simulation of the Influence of DE3 Tide on Nitric Oxide Infrared Cooling, *J.*
461 *Geophys. Res.: Space Phys.*, 125, e2019JA027131, <https://doi.org/10.1029/2019ja027131>, 2020.

462 Ren, Z., Wan, W., Xiong, J., and Liu, L.: Simulated wave number 4 structure in equatorial F-region vertical plasma drifts, *J.*
463 *Geophys. Res.: Space Phys.*, 115, A05301, <https://doi.org/10.1029/2009ja014746>, 2010.

464 Richmond, A. D.: Ionospheric Electrodynamics Using Magnetic Apex Coordinates, *J. Geomagn. Geoelectr.*, 47, 191–212,
465 <https://doi.org/10.5636/jgg.47.191>, 1995.

466 Rind, D., Suozzo, R., Balachandran, N. K., and Prather, M. J.: Climate change and the middle atmosphere Part I: The doubled
467 CO₂ climate, *J. Atmos. Sci.*, 47(4), 475–494, [https://doi.org/10.1175/1520-0442\(1998\)011<0876:CCATMA>2.0.CO;2](https://doi.org/10.1175/1520-0442(1998)011<0876:CCATMA>2.0.CO;2), 1990.

468 Roble, R. G. and Dickinson, R. E.: How will changes in carbon dioxide and methane modify the mean structure of the
469 mesosphere and thermosphere?, *Geophys. Res. Lett.*, 16, 1441-1444, <https://doi.org/10.1029/GL016i012p01441>, 1989.

470 Roble, R. G., Ridley, E. C., Richmond, A. D., & Dickinson, R. E.: A coupled thermosphere/ionosphere general circulation
471 model, *Geophys. Res. Lett.*, 15(12), 1325–1328, <https://doi.org/10.1029/g1015i012p01325>, 1988

472 Solomon, S. C., Liu, H. L., Marsh, D. R., McInerney, J. M., Qian, L., and Vitt, F. M.: Whole Atmosphere Simulation of
473 Anthropogenic Climate Change, *Geophys. Res. Lett.*, 45(3), <https://doi.org/10.1002/2017GL076950>, 2018.

474 Solomon, S. C., Qian, L., and Roble, R. G.: New 3-D simulations of climate change in the thermosphere, *J. Geophys. Res.:*
475 *Space Phys.*, 120(3), 2183-2193, <https://doi.org/10.1002/2014ja020886>, 2015

476 Sun, R., Gu, S., Dou, X., and Li, N.: Tidal Structures in the Mesosphere and Lower Thermosphere and Their Solar Cycle
477 Variations, *Atmosphere*, 13(12), 2036, <http://dx.doi.org/10.3390/atmos13122036>, 2022

478 Vogt, J., Sinnhuber, M., Kallenrode, MB.: Effects of Geomagnetic Variations on System Earth, in: *Geomagnetic Field*
479 *Variations, Advances in Geophysical and Environmental Mechanics and Mathematics*, Springer, Berlin, Heidelberg,
480 https://doi.org/10.1007/978-3-540-76939-2_5, 2009.

481 Weimer, D. R.: A flexible, IMF dependent model of high-latitude electric potentials having “space weather” applications,
482 *Geophys. Res. Lett.*, 23(18). <https://doi.org/10.1029/96GL02255>, 1996

483 Yue, J., Wang, W., Richmond, A. D., Liu, H.-L., and Chang, L. C.: Wavenumber broadening of the quasi 2 day planetary
484 wave in the ionosphere, *J. Geophys. Res.: Space Phys.*, 118, 3515–3526, <https://doi.org/10.1002/jgra.50307>, 2013

485 Yue, X., Cai, Y., Ren, Z., Zhou, X., Wei, Y., and Pan, Y.: Simulated Long-Term Evolution of the Ionosphere During the
486 Holocene, *J. Geophys. Res.: Space Phys.*, 127, e2022JA031042, <https://doi.org/10.1029/2022ja031042>, 2022.

487 Yue, X., Hu, L., Wei, Y., Wan, W., and Ning, B.: Ionospheric trend over Wuhan during 1947–2017: Comparison between
488 simulation and observation, *J. Geophys. Res.: Space Phys.*, 123, 1396–1409, <https://doi.org/10.1002/2017JA024675>, 2018

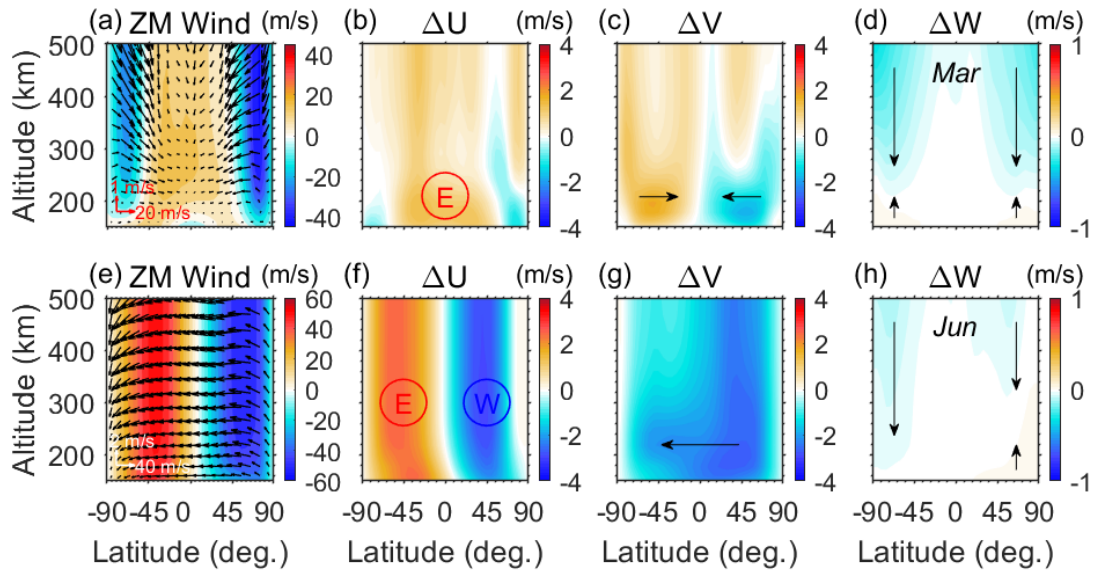
489 Zhang, S.-R., Holt, J. M., Erickson, P. J., Goncharenko, L. P., Nicolls, M. J., McCreedy, M., and Kelly, J.: Ionospheric ion
490 temperature climate and upper atmospheric long-term cooling, *J. Geophys. Res.: Space Phys.*, 121, 8951–8968.
491 <https://doi.org/10.1002/2016JA022971>, 2016

492 Zhang, R., Liu, L., Liu, H., Le, H., Chen, Y., and Zhang, H.: Interhemispheric transport of the ionospheric F region plasma
493 during the 2009 sudden stratosphere warming, *Geophys. Res. Lett.*, 47, e2020GL087078,
494 <https://doi.org/10.1029/2020GL087078>, 2020

495 Zhou, X., Yue, X. A., Liu, H. L., Wei, Y., and Pan, Y. X.: Response of atmospheric carbon dioxide to the secular variation of
496 weakening geomagnetic field in whole atmosphere simulations, *Earth and Planetary Physics*, 5(4), 327–336,
497 <https://doi.org/10.26464/epp2021040>, 2021

498 Zhou, X., Yue, X., Ren, Z., Liu, Y., Cai, Y., Ding, F., and Wei, Y.: Impact of Anthropogenic Emission Changes on the
499 Occurrence of Equatorial Plasma Bubbles, *Geophys. Res. Lett.*, 49, e2021GL09735, <https://doi.org/10.1029/2021gl097354>,
500 2022.

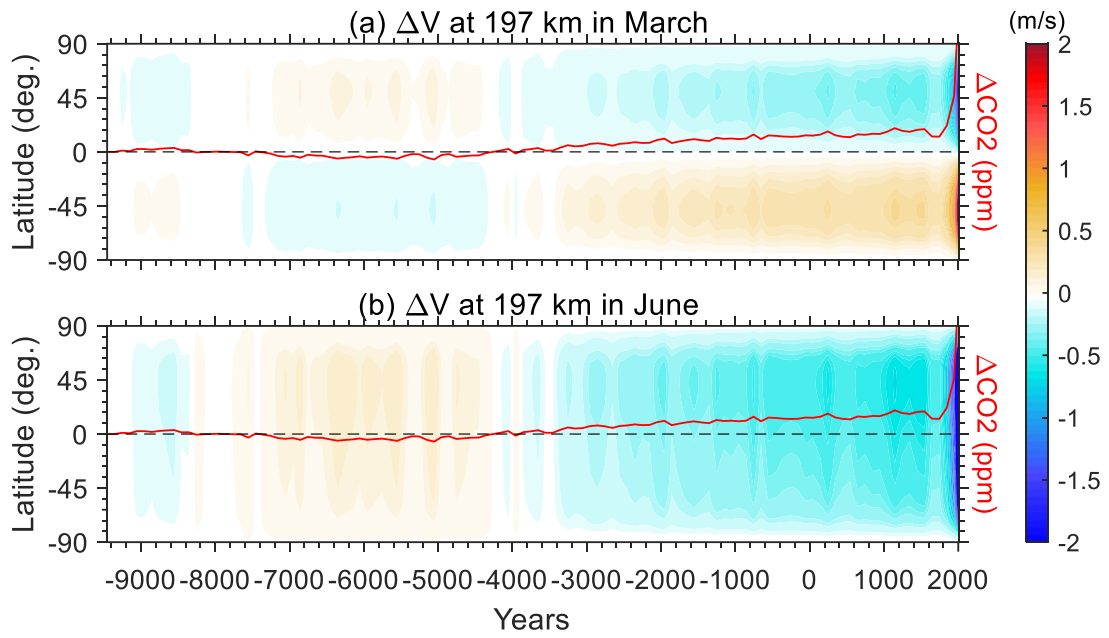
- 501 Zhong, J., Wan, W. X., Wei, Y., Fu, S. Y., Jiao, W. X., Rong, Z. J., et al.: Increasing exposure of geosynchronous orbit in solar
502 wind due to decay of Earth's dipole field, *J. Geophys. Res.: Space Phys.*, 119, 9816–9822,
503 <https://doi.org/10.1002/2014JA020549>, 2014
- 504 Zossi, B. S., Elias, A. G., and Fagre, M.: Ionospheric conductance spatial distribution during geomagnetic field reversals, *J.*
505 *Geophys. Res.*, 123(3), 2379–2397, <https://doi.org/10.1002/2017JA024925>, 2018
- 506



507

508 **Figure 1.** (a) Thermospheric circulation is illustrated by ~~contours-colors~~ (zonal) and ~~arrows~~ (meridional and vertical) in
 509 March 2015. (b)–(d) Changes in zonal, meridional and vertical wind velocity due to the increase of CO₂ from 1945 to 2015.
 510 Plots (e)–(f) are the same as plots (a)–(d) but for June.

511

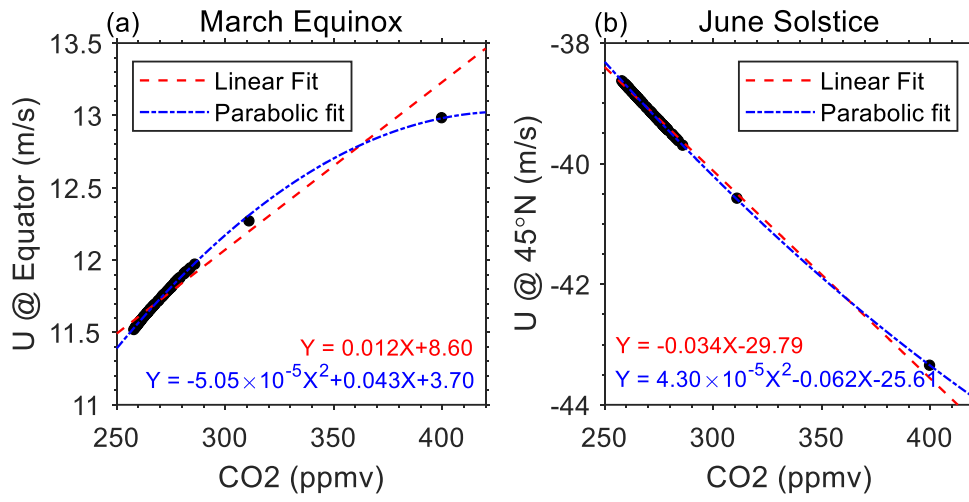


512

513 **Figure 2.** Time evolution of the changes in the zonal-mean meridional wind at 197 km during (a) March and (b) June. The
 514 corresponding CO2 variation is plotted in the red solid line.

515

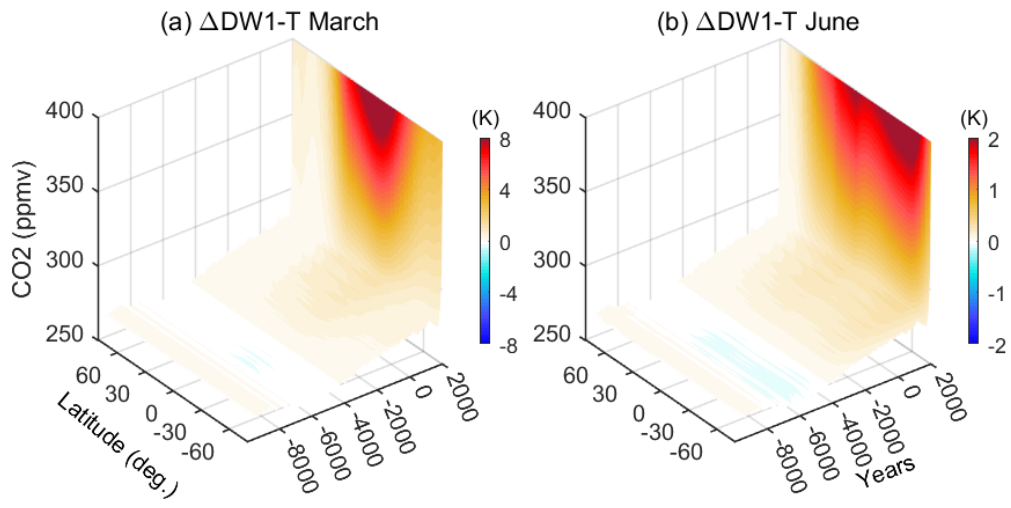
516



517

518 **Figure 3.** Response of thermospheric zonal-mean zonal winds (150–600 km average) to the CO2 increase (a) at the equator in
 519 the March equinox. (b) at 45°N in the June solstice. Linear and parabolic fitting are indicated in red-dashed and blue-dash-
 520 dotted lines, respectively.

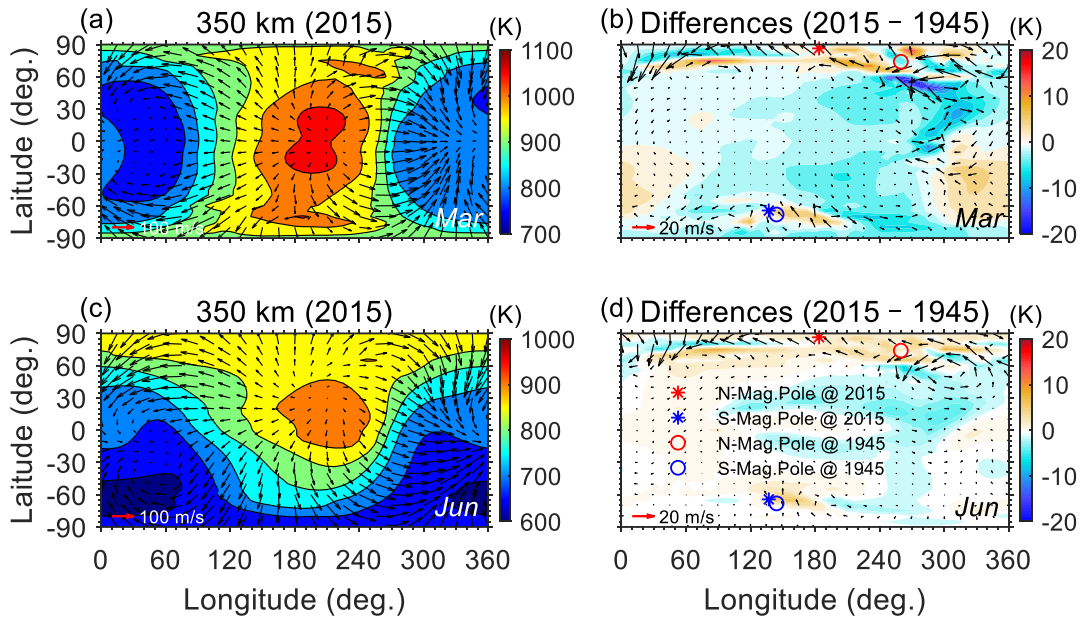
521



522

523 **Figure 4.** Change in the amplitude of diurnal migrating tide (DW1) at 240 km due to the CO₂ variation in (a) March and (b)
 524 June with respect to the beginning of the simulation.

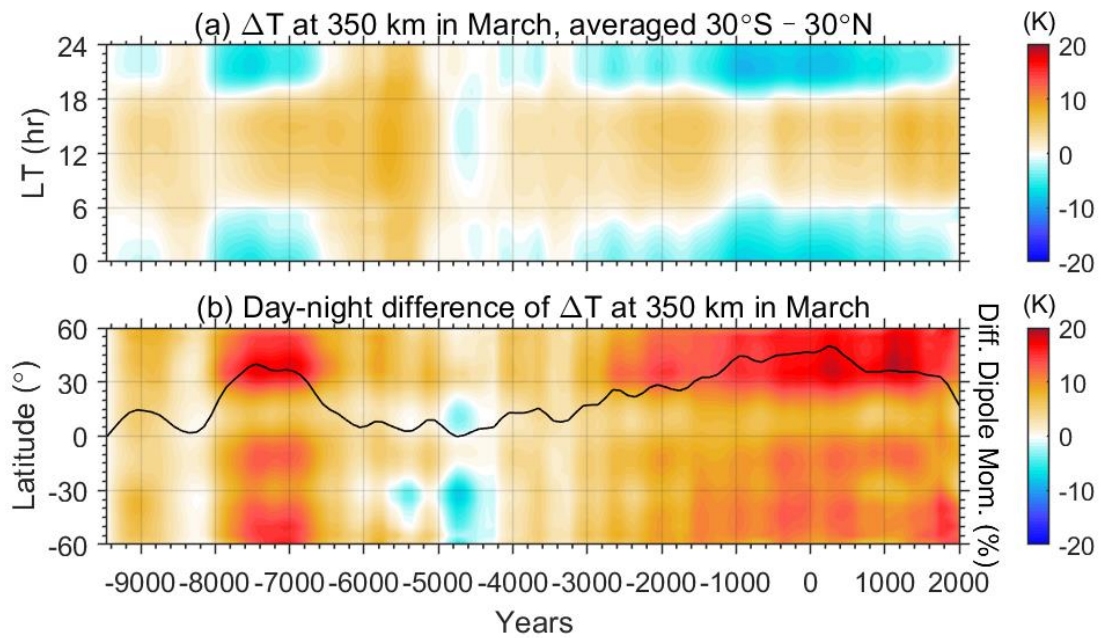
525



526

527 **Figure 5.** Geographic distribution of neutral temperature (color contours,) and horizontal winds (black arrows) at 350 km in
 528 (a) March and (c) June at UT00. (b) Differences in neutral temperature and horizontal winds due to changes in geomagnetic
 529 field between 1945 and 2015. The scales of wind velocity are indicated in the lower-left corner of each plot. The changes of
 530 north and south magnetic poles between 1945 and 2015 are illustrated in plots (b) and (d).

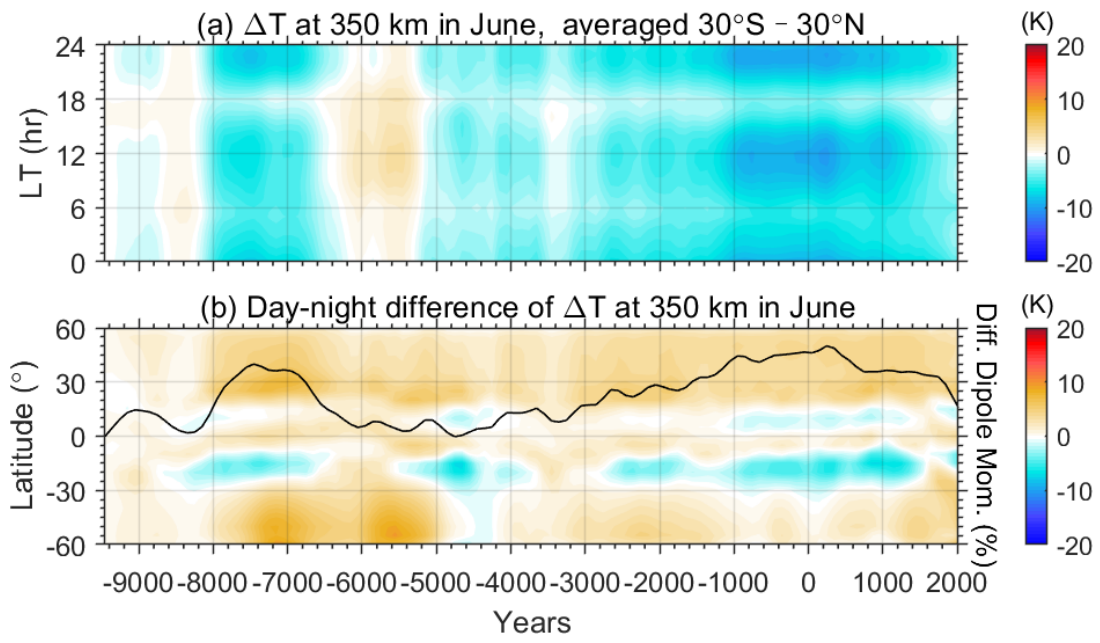
531



532

533 **Figure 6.** (a) Local-time (LT) variation of the zonal-mean temperature changes at low latitudes (30°S–30°N) caused by the
 534 secular variation of geomagnetic fields at 350 km in March during the Holocene. (b) Latitudinal variation of day-night
 535 differences in the zonal-mean temperature during March plotted versus year and with respect to the beginning of the simulation.
 536 The daytime and nighttime are corresponding to LT10–14 and LT22–02, respectively. Relative change of the geomagnetic
 537 dipole moment is plotted in the black-solid line in plot (b).

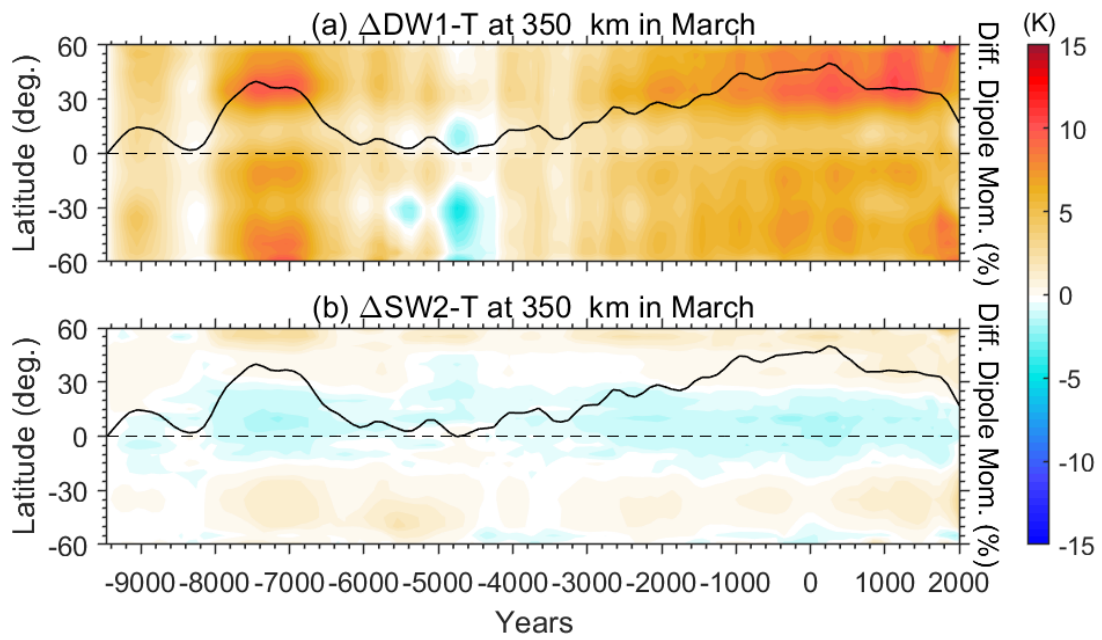
538



539

540 **Figure 7.** Same as Figure 6, but for the case of June.

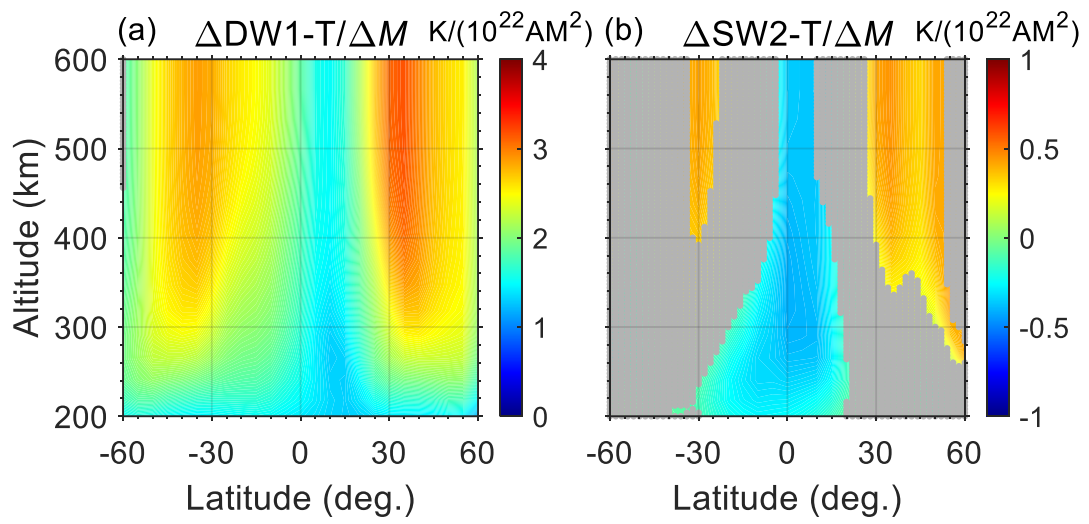
541



542

543 **Figure 8.** Time evolution of the differences in the amplitude of (a) DW1 and (b) SW2 with respect to the beginning of the
 544 simulation.

545



546

547 **Figure 9.** Coefficient estimates for the linear regression of (a) DW1-T and (b) SW2-T amplitudes on the geomagnetic dipole
 548 moment. The grey shaded area indicates where the absolute values of correlation coefficients are less than 0.6.

549

550

551